

Scalable Fabrication of Silicon-Graphite Microsphere by Mechanical Processing for Lithium-Ion Battery Anode with Large Capacity and High Cycling Stability

Qiuyan Shen,^[a, b] Ruibing Zheng,^[c] Yingying Lv,*^[b] Yanyan Lou,^[a] Liyi Shi,^[b, d] and Shuai Yuan*^[b]

In order to combine the high stability of graphite and the large theoretical capacity of silicon, silicon-graphite composites attract tremendous attentions. However, the cycling stability is still a bottleneck hindering their commercialization due to the large volume expansion and poor interface compatibility. In this study, the bead grinding method is used to break micro-sized silicon and graphite particles by strong shear force simultaneously, inducing the solid-solid interface reaction between fresh silicon nanoparticles and graphite nanosheets. Subsequently, an evaporation induced self-assembly happens in spray drying process, allow for scalable synthesis of Si-graphite

microsphere. The silicon-graphite microsphere (Si-G microsphere) delivers an excellent cycling performance, with a reversible capacity of 1895 mAh g^{-1} at a current density of 0.5 A g^{-1} over 500 cycles and a capacity retention of 99.8%. Moreover, the pouch-type full battery of Si-G microsphere/graphite||LiNi_{0.5}Co_{0.2}Mn_{0.3}O₂ exhibits remarkable cycling stability with the capacity retention of 79.3% after 800 cycles. The manufacture process using commercial raw materials and simple mechanical strategy demonstrates great potential for the low-cost and scaled synthesis of high-performance silicon-graphite anodes.

Introduction

As the emerging market of portable electronic devices and electric powered vehicles, even the advent of electric powered aircrafts in the future, there is a fast growing demand for lithium-ion batteries (LIBs) with high energy density and long cycle stability.^[1–3] Silicon (Si) is the next-generation anode material, owing to the advantages of high theoretical capacity (4200 mAh g^{-1} , ten times higher than that of conventional graphite anodes), abundant reserves on the earth, low cost and reasonable voltage platform (below 0.5 V vs. Li/Li⁺).^[4,5] However, silicon anode suffers from the huge volume expansion (~400%) during lithiation, structural collapse caused by the delithiation and poor electrical conductivity, thus, the poor

electrochemical performance of which hinders the commercial application.^[6,7]

In order to solve the above problems, numerous strategies have been developed. Nano-sized silicon, like silicon nanowires,^[8] nanotubes,^[9,10] nanoparticles,^[11] perform increased cycle life of battery due to the reduced mechanical fracture of Si. The composite structure would provide enough space for accommodating large volume variations and buffering volume effect, such as porous or hollow structures,^[12,13] yolk-shell structures^[14,15]. Combining with carbon substrates^[16,17] can also release the stress in the process of volume expansion. Graphite with low cost and great electron conductivity is considered as one of the most suitable substrates.^[18] Recently, much research on synthetic strategies of Si/graphite composite has been reported, demonstrating outstanding capacity and the excellent stability.^[19] Li et al. prepared micro-nano structured composite, in which graphite coated by ZnO-incorporated and carbon-coated silicon shell via a method of liquid phase self-assembly and following annealing treatment. The composite anode delivered a stable long-cycling life of 1000 cycles with reversible capacity of 1150 mAh g^{-1} at a current density of 0.6 A g^{-1} .^[20] Luo et al. reported a porous silicon/graphite/carbon composite by a surface modification method, which performed a reversible specific capacity of approximate 378 mAh g^{-1} after 500 cycles at a current density of 0.372 A g^{-1} after pre-lithiation.^[21] Xu et al. prepared a Si/spent graphite composite through ball milling. The organic components of spent graphite improved the mechanical flexibility and the stability of SEI (solid electrolyte interface) layer, demonstrating a capacity retention of 69% at a current density of 1.0 A g^{-1} after 400 cycles.^[22] Parekh et al. prepared a Si-carbon-graphite composite through ball milling, which derived an amorphous carbon to

[a] Q. Shen, Y. Lou
School of Materials Science and Engineering,
Shanghai University
Shanghai 200444, China

[b] Q. Shen, Assoc. Prof. Y. Lv, Prof. L. Shi, Prof. S. Yuan
Research Center of Nanoscience and Nanotechnology,
Shanghai University
Shanghai 200444, China
E-mail: yingylv@shu.edu.cn
s.yuan@shu.edu.cn

[c] R. Zheng
Zhejiang Kaihua Yuantong Silicon Industry Co., LTD
Zhejiang 311600, China

[d] Prof. L. Shi
Emerging Industries Institute,
Shanghai University
Zhejiang 314006, China

 Supporting information for this article is available on the WWW under
<https://doi.org/10.1002/batt.202200186>

 An invited contribution to a Special Collection on IV Symposium on Advanced Energy Storage

improve the interfacial binding. The capacity of 448 mAh g^{-1} at a current density of 0.5 A g^{-1} after 100 cycles was retained, profiting from the interconnected architecture.^[23] While improving cycle stability has been achieved for the silicon/carbon composites, most studies with a fast capacity decay are incompatible in industry. Increased ion transportation rate and enhanced electron conductivity can be achieved for nanoscaled anode materials. However, too densely packed nano-material may induce poor utilization inside the electrode, leading to low energy density at a high loading amount. Hence, developing micro-sized electrode materials could be good choices with the balance for high energy density and electrochemical stability.

Based on the above views, the Si-graphite microsphere with nano-sized silicon and few-layered graphite is fabricated at a large scale, through a simple two-step mechanical strategy of bead grinding and spray drying (Figure 1a). Firstly, layer structured nanocomposites with silicon nanoparticles and graphite nanosheets are obtained in the bead grinding process, where the commercial micro-sized silicon and graphite particles

are broken simultaneously by strong shear force. The homogeneously distributed silicon nanoparticles and graphite nanosheets are tightly connected with each other by Si-C covalent bonds. Subsequently, the Si-graphite microsphere is prepared by spray-drying through an evaporation induced self-assemble process. In the Si-graphite microsphere, the few-layered graphite nanosheets could provide a conductive frame and play a buffer role for the expansion of nanosized silicon. In addition, the micro-sized spheroidal structure would show isotropic expansion. The Si-graphite spheroidal anode material (Si-G microsphere) delivers an excellent cycling performance, with a reversible capacity of 1895 mAh g^{-1} at a current density of 0.5 A g^{-1} and a capacity retention of 99.8% over 500 cycles. The pouch-type full battery assembled with the Si-G microsphere/graphite as anode and LiNi_{0.5}Co_{0.2}Mn_{0.3}O₂ (NCM523) as cathode maintains 79.3% of the reversible capacity after 800 cycles. This study reveals possible scalable and low-cost synthetic strategy for silicon graphite composite with high capacity and long cycle stability.

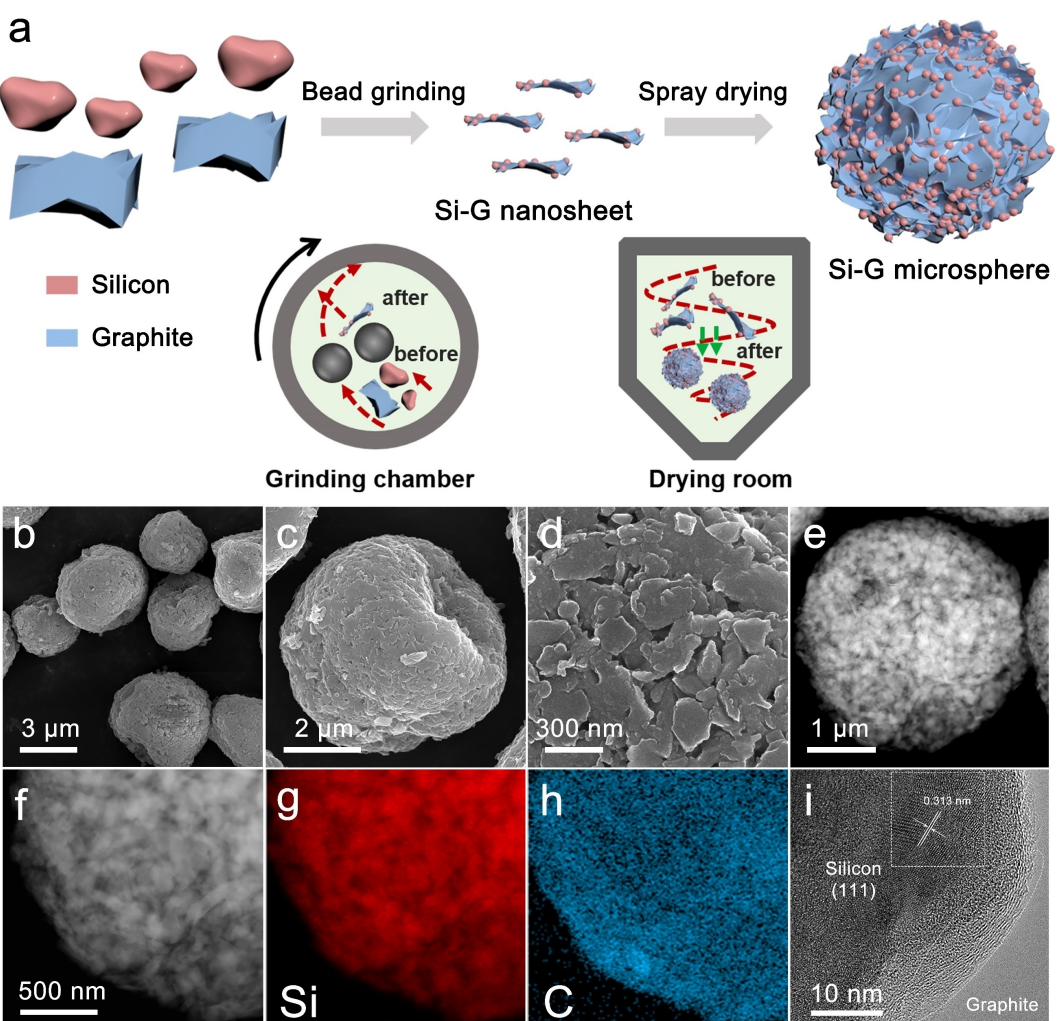


Figure 1. a) The synthesis diagram of nanostructured Si–G microsphere through a two-step mechanical strategy, showing the micro-sized spheroidal morphology and the interior nanostructure. b–d) SEM images of Si–G microsphere at different magnification exhibiting regular spheroidal morphology and lamellar accumulated surface. e) TEM image of Si–G microsphere. f–h) EDX images of Si–G microsphere showing uniform element distribution. i) HRTEM image of Si–G microsphere.

Results and Discussion

The break-dispersion-assemble synthetic route of nanostructured Si–G microsphere is schematically displayed in Figure 1a. Briefly, commercial micron-sized silicon and graphite particles are used directly. Through a solid reaction at bead grinding system, the particle size of silicon is dramatically reduced to nanometer size by the strong shear force of grinding beads. Meanwhile, few-layered graphite sheet is obtained ascribe to the breakage of Van der Waals force at the solid reaction process. Ascribed to the solid-solid interface reaction by high-speed mechanical activation, the resulting silicon nanoparticles are embedded on the graphite nanosheet, which is denoted as Si–G nanosheet. Through a spray drying process, the droplet containing silicon-graphite nanosheets are dispersed into a drying chamber and rapidly dried within a few seconds. The as-synthesized sample denoted as Si–G microsphere is collected and used for following test directly.

Different with the pristine commercial silicon's rough surfaces and irregular morphology (Figure S2), the as-synthesized Si–G microsphere has a regular spheroidal morphology with an average diameter of around 6 μm . (Figure 1b and c). The surfaces of Si–G microsphere are covered by loose-packed uniform lamellar fragments with a size of several hundred nanometers (Figure 1d), which should be derived from the self-assembly of Si–G nanosheets (Figure S3a–c). The TEM (transmission electron microscopy) images reveal that the microspheres are composed of interconnected nanoparticles and nanosheets (Figure 1e). Detailed EDX (energy-dispersive X-ray spectroscopy) images demonstrate uniformly distributed elements of silicon and carbon (Figure 1f–h). HRTEM (high-resolution transmission electron microscopy) image reveals a single-crystal structure with clear lattice fringes of $\sim 0.313 \text{ nm}$ spacing, which corresponds to the silicon's (111) plane. The silicon nanoparticles are closely covered by few-layered graphite nanosheets (Figure 1i), even in a larger domain (Figure S3d). Such a micrometer-sized Si–G sphere is formed by tightly interconnected Si–G nanosheets.

The wide-angle XRD patterns show characteristic diffraction peaks at 28.4° , 47.3° , 56.2° , 69.1° , 76.4° and 88.0° , which can be assigned to the (111), (220), (311), (400), (331) and (422) crystal plans of silicon (Figure 2a) (JCPDS card no. 27-1402), respectively. For Si–G nanosheet and Si–G microsphere, the peak centered at 26.4° is well matched with characteristic lattice plane (002) of graphite (JSPDS card no. 26-1079), verifying the existence of graphite. The surface chemical composition of the samples is further investigated by X-ray photoelectron spectroscopy (XPS) (Figures 2b and S4), revealing the existence of Si, C and O elements. Three peaks of Si 2p at 99.4 eV, 101.8 eV and 103.4 eV should be derived from Si–Si, Si–C and Si–O bonds (Figure 2b). The existence of Si–C bond proves that silicon and graphite is tightly crosslinked by covalent bond, which is consistent with the TEM images at Figure 1(i). The Si–O bond should be ascribed to SiO_x on the surface of silicon nanoparticles due to the partial oxidation by air or water. The as-formed oxide layer would prevent the exposure of unstable silicon surface in the electrolyte, and result in a stable SEI

layer.^[24] Before grinding, HRTEM images show the clear crystallized structured graphite and silicon of the mixture (Figure 2c). After bead grinding, there is no distinct boundary between silicon and graphite (Figure 2d) in Si–G nanosheet. AFM (atomic force microscopy) is conducted to measure the thickness of graphite sheets after a hydrofluoric acid etching (Figure 2e and f). AFM results demonstrate that all of the graphite sheets are laid on one plane, which further confirm the uniformity in the solid reaction process. The average width of the graphite sheets is about $0.8 \mu\text{m}$, and the average thickness of which is about 1.5 nm. Obviously, few tiny holes on the surfaces can be observed, which illustrate that silicon nanoparticles may be embedded into the graphite sheet during solid-solid reaction. The few-layered graphite nanosheet with better mechanical flexibility can buffer the expansion of silicon, compared with the rigid micrometer sized graphite particles.^[25] Moreover, Si–G nanosheet ($2.88 \times 10^{-2} \mu\text{S cm}^{-1}$) shows higher conductivity than commercial Si ($2.02 \times 10^{-3} \mu\text{S cm}^{-1}$), verifying the tight connection between silicon nanoparticles and few-layered graphite.

The initial charge/discharge curves are measured at a current density of 0.1 A g^{-1} between 0.01 V and 1.5 V, illustrating the characteristic (de)lithiation plateaus of silicon anodes (Figure 3a). The Coulombic efficiency (CE) at the first cycle of Si–G nanosheet, Si–G microsphere anodes are 87.6% and 82.4%, respectively. Both of them are higher than that of commercial Si anode (78.2%), which should be ascribed to the formation of SEI layer. The cycling curves and Coulombic efficiency curves of commercial Si, Si–G nanosheet and Si–G microsphere anodes are shown in Figure 3b. After being activated at a current density of 0.1 A g^{-1} for two cycles, commercial Si, Si–G nanosheet, Si–G microsphere anodes are cycled at a higher current density of 0.5 A g^{-1} , performing initial capacity of 2290 mAh g^{-1} , 2209 mAh g^{-1} , 1899 mAh g^{-1} , respectively. Si–G microsphere anode maintains a discharge capacity of 1895 mAh g^{-1} after 500 cycles, which is much higher than that of commercial Si anode (470 mAh g^{-1}) and Si–G nanosheet anode (809 mAh g^{-1}). The high capacity retention of over 99% and large discharge capacity (1895 mAh g^{-1}) at a current density of 0.5 A g^{-1} after 500 cycles of Si–G microsphere anode should be ascribed to that the layered graphite nanosheets can afford the huge volume change of silicon. The charge/discharge curves of Si–G microsphere anode (Figure 3c) at 1st, 100th, 300th and 500th cycle have no obvious change, exhibiting that the microsphere composite maintains great mechanical stability during the long cycling. The lower charge transfer resistance with the Si–G microsphere anode (70.8 ohm) in contrast to the Si–G nanosheet anode (159.3 ohm) and commercial Si anode (233.2 ohm) after 300 cycles from the EIS (Electrochemical impedance spectroscopy) results (Figure 3d and e), implying that the enhanced charge transfer kinetics (Figure S6), which should be ascribed to the particles by layer nanostructure and the micrometer-sized spheroidal morphology. After 500 cycles, there is only a slight increase on the transfer resistance of Si–G microsphere. The surfaces of the Si–G microsphere are covered by ultra thin graphite/ SiO_x layer, which work as a protection for uncontrollable growth of SEI layer on the silicon surfaces.

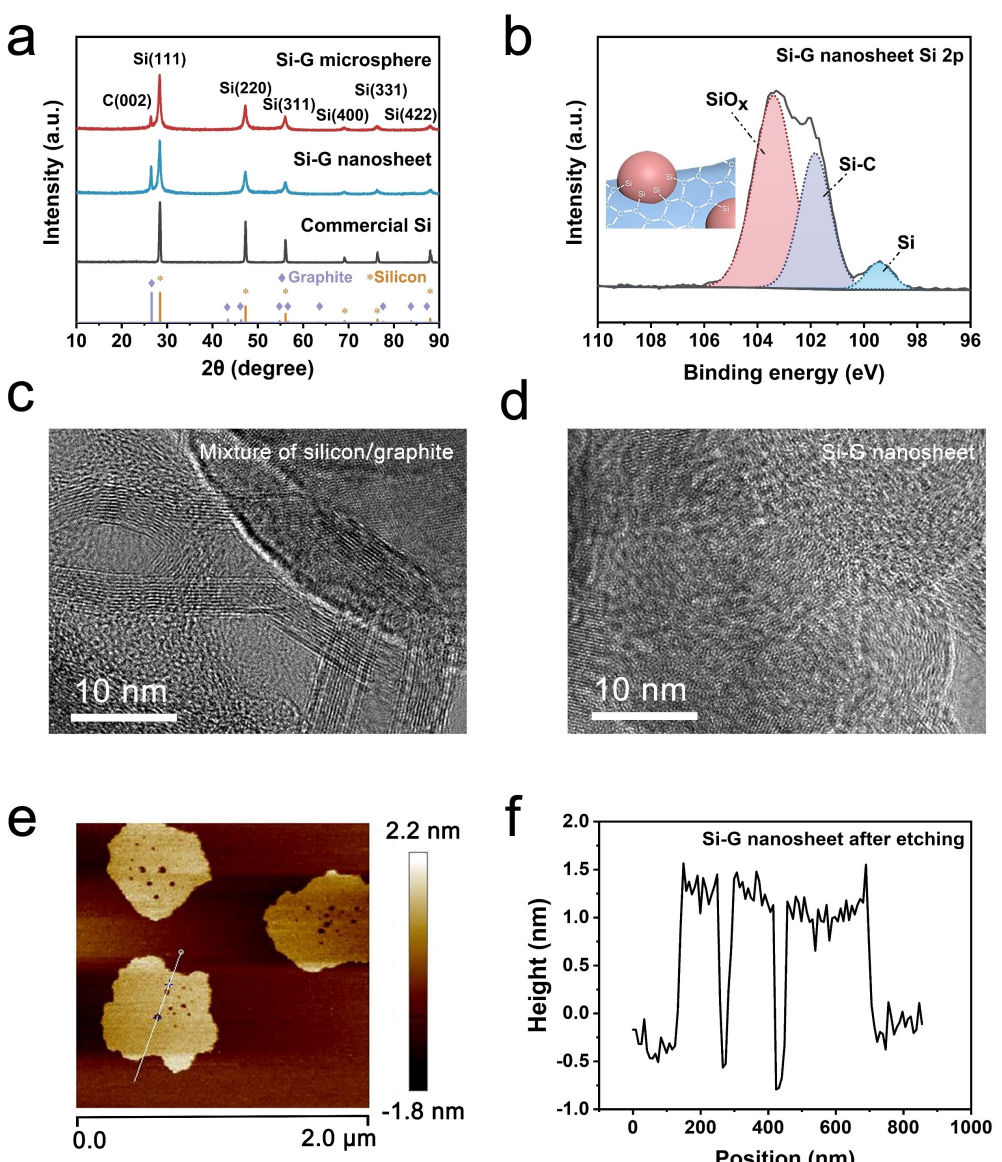


Figure 2. a) The XRD patterns of commercial Si, Si–G nanosheet, Si–G microsphere. b) The XPS spectrum of Si–G nanosheet displays a strong Si–C covalent bond. c and d) HRTEM images of mixture of silicon/graphite and Si–G nanosheet. e and f) AFM image of silicon particle etched thin graphite by hydrofluoric acid and the height profiles curve.

Moreover, the spheroidal structure, which is assembled by tightly wrapped silicon nanoparticles and few-layered graphite sheets, could prevent the detachment of silicon particles after long cycling. The discharge capacity at the current densities varied from 0.1 A g^{-1} to 4.0 A g^{-1} are demonstrated in Figure 3(f) and Table S2. Si–G nanosheet and Si–G microsphere anodes present a higher capacity (419 mAh g^{-1} , 400 mAh g^{-1}) than that of commercial Si anode (8 mAh g^{-1}) after 10 cycles at a high current density of 4.0 A g^{-1} . The superior rate capability should be ascribed to the rapid diffusion of lithium-ion and transmission of electrons in the composite structure. When the current density reverts to 0.1 A g^{-1} , the capacity of Si–G microsphere anode recovers to 2541 mAh g^{-1} , which is higher than that of Si–G nanosheet anode (2214 mAh g^{-1}).

The CV (cyclic voltammetry) measurement for Si–G microsphere anode at a scanning rate of 0.5 mV s^{-1} is shown in Figure S7. A long and flat voltage plateau at $0.1\text{--}0.2 \text{ V}$ is mainly associated with the formation of Li_xSi and Li_xC . The voltage plateaus around 0.05 V and 0.25 V should be corresponding to Li^+ extraction. In the discharge curve, two peaks at 0.38 V and 0.52 V are corresponding to the alloying behavior of Li_xSi . From the 3rd cycle, the similar redox peak area suggests that SEI layer tends to be stable in the first two cycles. The statistics on performance comparison between our Si–G microsphere and the other silicon-graphite composites in the past 15 months (from 2021-01-01 to 2022-03-01) are shown in Figure 3g and Table S3. Compared with the above data, Si–G microsphere anode performs superior high capacity and long cycle stability

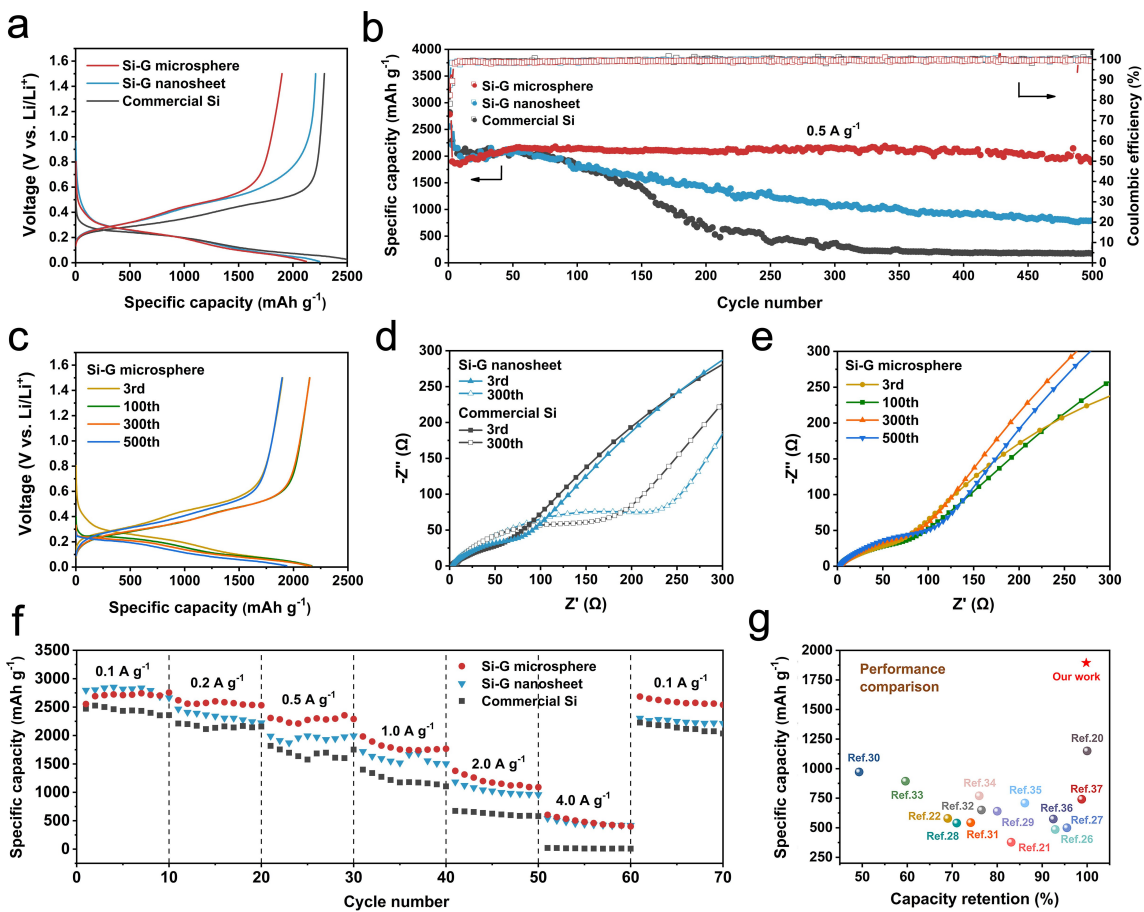


Figure 3. a) The initial charge/discharge curves of commercial Si, Si–G nanosheet, Si–G microsphere anodes at a current density of 0.1 A g⁻¹. b) Cycling performance of commercial Si, Si–G nanosheet, Si–G microsphere anodes at a current density of 0.5 A g⁻¹ (activate at a current density of 0.1 A g⁻¹ for the first two cycles). c) The charge/discharge curves of Si–G microsphere anode at the 3rd, 100th, 300th and 500th cycle. d) Electrochemical Impedance measurements of commercial Si, Si–G nanosheet anodes after the 3rd and 300th cycles. e) Electrochemical Impedance measurements of Si–G microsphere anode after the 3rd, 100th, 300th, 500th cycles. f) Rate capability of commercial Si, Si–G nanosheet, Si–G microsphere anodes at the current density varied from 0.1 A g⁻¹ to 4.0 A g⁻¹. g) The Statistics on performance comparison between our Si–G microsphere and the other silicon-graphite composites in the past 15 months (2021-01-01-2022-03-01).^[26-37]

(the reversible capacity of 1895 mAh g⁻¹ and capacity retention of 99.8% after 500 cycles).

The Si–G microsphere anode has a strong mechanical stability, the spheroidal morphology of which is maintained after 500 cycles (Figure 4*i* and *j*). There are dramatic cracks in the commercial Si anode (Figure 4*a* and *b*) after 500 cycles. Si–G nanosheet anode (Figure 4*e* and *f*) show the formation of agglomeration accompanied by lots of slight cracks after cycling. Moreover, due to the irregularity of Si–G nanosheet, the anode shows partial agglomeration on the surface and uneven expansion on the cross-sectional side image. Interestingly, Si–G microsphere anode maintains obvious spheroidal morphology after 500 cycles at a current density of 0.5 A g⁻¹. The spheroidal layered structure of Si–G microsphere is helpful in keeping the structural integrity during cycling, which confirm the existence of the compact bond between silicon and graphite, exhibiting stronger particle cohesion. The initial cross-sectional thickness of the three materials is about 18 μm. After 500 cycles, there is the smallest thickness change for Si–G microsphere anode, increase of which is about 145%

(Figure 4*k* and *l*). Whereas the thicknesses of commercial Si and Si–G nanosheet anodes are increased to 297% (Figure 4*c* and *d*) and 208% (Figure 4*g* and *h*), respectively. Therefore, the spheroidal layered structure alleviates the isotropic volume effect in all directions. Therefore, the spheroidal micro-sized Si–G microsphere allows the enough penetration of the electrolyte from all direction. Meanwhile, the interior space would provide sufficient pathways for fast diffusion of Li⁺ ions, and the interconnected graphite nanosheets could also accommodate large volume change of silicon nanoparticles. The EDX images of the Si–G microsphere are shown in Figure 4(*m-o*) to judge the particle composition after cycling. The element mapping images reveal that silicon and carbon are still homogeneously distributed throughout the whole particle, showing that silicon and graphite is still tightly rolled together even after 500 cycles. The pores of particles could provide enough space for the volume change of silicon (Figures 4*p* and S5). Thus, it is an effective way to improve extremely large reversible capacity through the spheroidal layered structure construction. The silicon-graphite microsphere that maintains

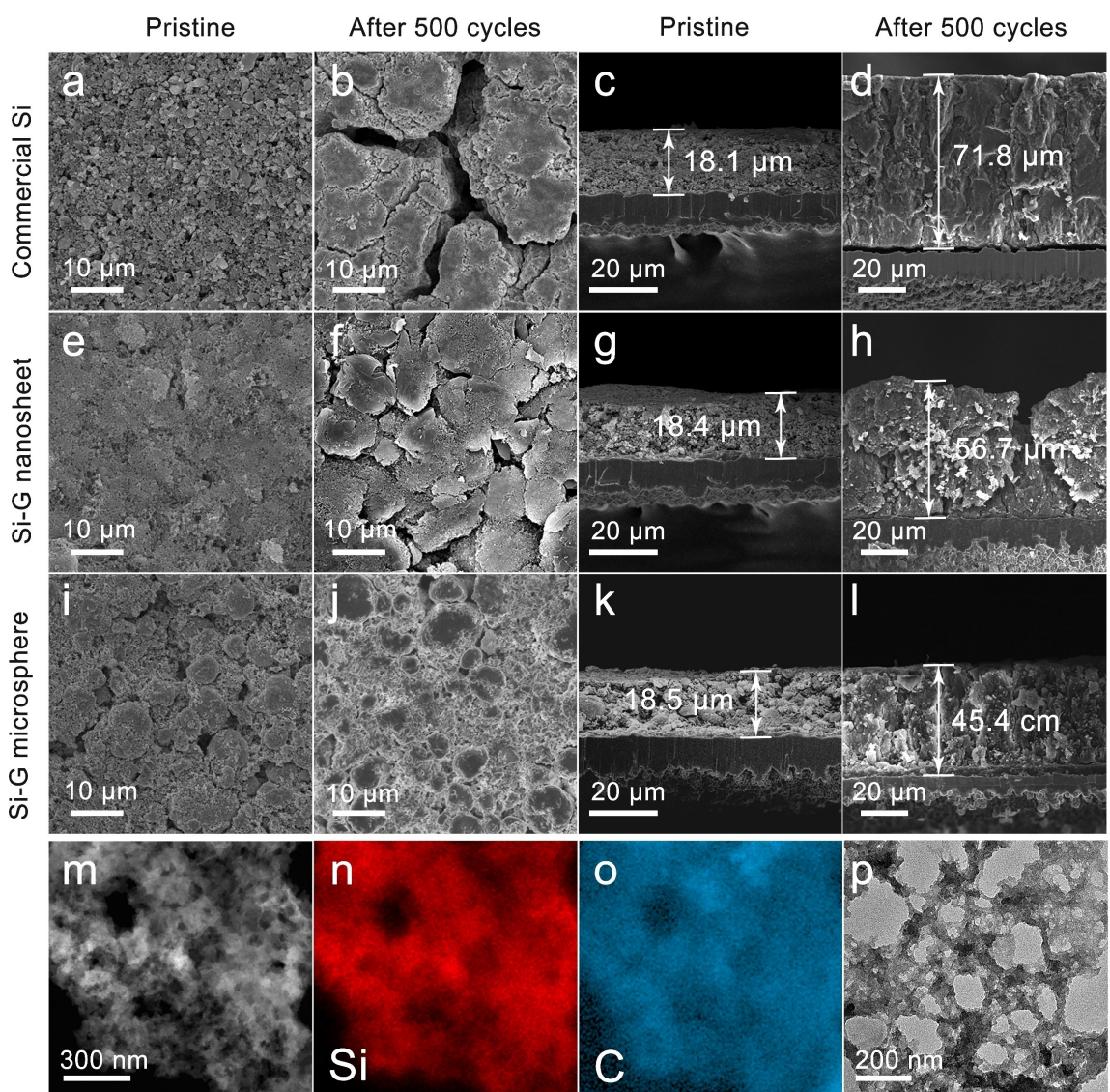


Figure 4. Surface SEM images of a and b) commercial Si, e and f) Si–G nanosheet, i and j) Si–G microsphere anodes before and after 500 cycles at a current density of 0.5 A g^{-1} , and cross-sectional SEM images of c and d) commercial Si, g and h) Si–G nanosheet, k and l) Si–G microsphere anodes before and after 500 cycles at a current density of 0.5 A g^{-1} . m and o) Elements distribution and p) TEM image of Si–G microsphere after 500 cycles at a current density of 0.5 A g^{-1} .

the spheroidal morphology even while suffering long-term cycling. The interconnected graphite nanosheets not only provides a highly conductive framework, but also has a strong mechanical strength for expansion of silicon nanoparticles.

The pouch-type full battery with a negative/positive (N/P) ratio of 1.1 using the $\text{LiNi}_{0.5}\text{Co}_{0.2}\text{Mn}_{0.3}\text{O}_2$ (NCM523) as cathode, Si–G microsphere mixed with graphite (mass ratio Si–G microsphere:graphite = 2.5:97.5) as anode are checked in the voltage range of 3.0 V to 4.2 V with a current density of 0.5 C (Figure 5a). An initial discharge capacity and CE of 823 mAh and 98.3% is demonstrated at Figure 5(b). The full battery exhibits good capacity retention, which is 83.2% after 500 cycles and 79.3% after 800 cycles (Figure 5c), along with a CE of 99.2% after initial 2 cycles, indicating the potential commercial application of silicon-graphite anode with large capacity and high cycling stability. For comparison, the rate-

performance of full battery at varied current densities are evaluated in Figure 5(d), which deliver the reversible capacity of 835 mAh, 814 mAh, 787 mAh, 749 mAh and 530 mAh at the rate of 0.5 C, 1.0 C, 2.0 C, 3.0 C and 5.0 C, respectively.

Conclusion

Through a scalable two-step mechanical strategy, Si-graphite microspheres are synthesized with low cost. Firstly, bead grinding process breaks the commercial micro-sized silicon or graphite to nano-sized particles and sheets, respectively. Moreover, the Si–C covalent bonds are created to improve the strong connection between silicon nanoparticles and few-layered graphite nanosheets. Secondly, spray drying process induces the assembly of Si nanoparticles and graphite nano-

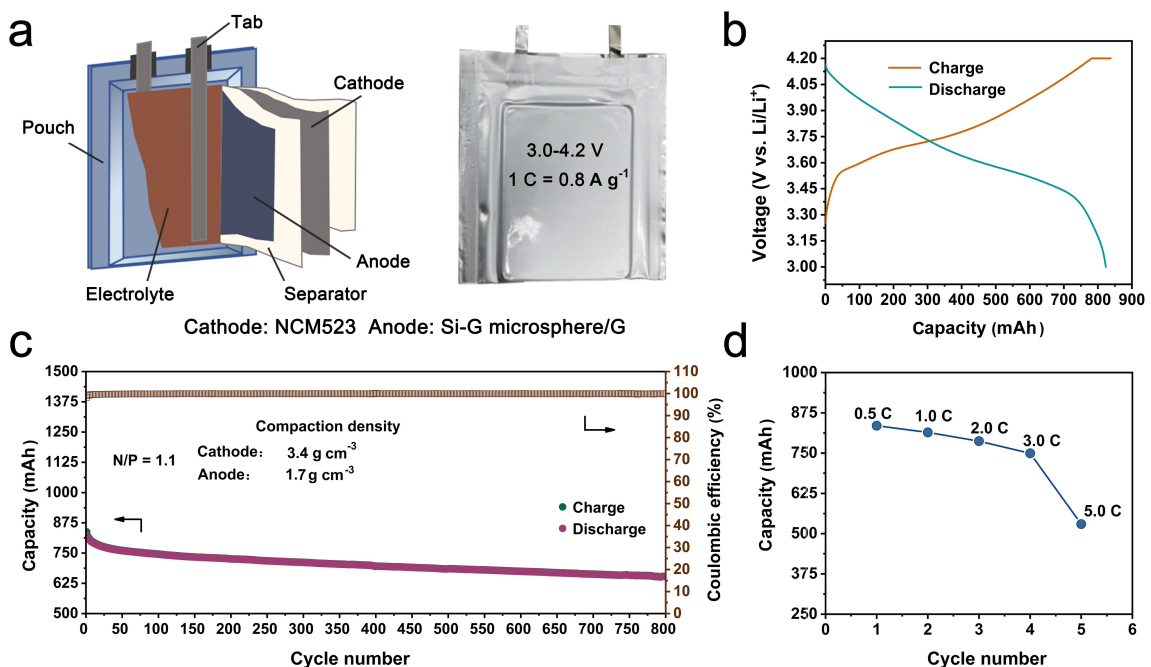


Figure 5. a) Schematic illustration and demonstration, b) initial charge/discharge curve, c) cycling performance and d) rate capacity of the pouch-type full battery using Si–G microsphere mixed with graphite as anode and NCM523 as cathode, respectively.

sheets to micro-sized spheres. The Si–G microsphere anode performs large capacity and highly cycling stability for 500 cycles. In this microsphere, the few-layered graphite nanosheets play as buffer layer to alleviate volume effect and build a conductive framework to enhance the electronic conductivity. Besides, the isotropic swelling further reduces the degradation of silicon particles. The full battery using Si–G microsphere/G anode coupled with NCM523 cathode still performs good capacity retention, which reaches 79.3% after 800 cycles, demonstrating a cost-effective, simple strategy for commercialization of high capacity, long cycle stability silicon-graphite anode.

Experimental Section

Material Synthesis

The materials synthesis is a two-step mechanical strategy (Figure S1), a grinding process using a bead miller. (PML-Easy TM, Bühler (Wuxi, China) Commercial Co., Ltd.), and a following drying process using a spray dryer (Mini Spray Dryer QZR.P-1, Wuxi Linzhou drying equipment Co., Ltd.). Commercial micro-meter sized silicon powder and graphite powder (Mass ratio of silicon:graphite = 8:1) were dispersed in 800 mL isopropanol and ground for 2.5 h. Then, re-dispersed in deionized water with 0.5 wt.% solid content. After stirring for 0.5 h, the dispersed suspension was dried by spray dryer at the inlet and outlet temperature of 240 °C and 130 °C for 6 h. The collected composite is denoted as Si–G microsphere. Preparing same solution according to a grinding procedure and drying by rotary evaporation at 40 °C for 12 h to obtain the powder named Si–G nanosheet for comparison.

Physical Characterizations

The surface and cross-sectional morphologies of as-obtained samples before and after cycling were performed by scanning electron microscope (SEM, JSM-7500F). Meanwhile, the microstructures and internal elements distribution were obtained on the transmission electron microscope and high-resolution transmission electron microscope (TEM/HRTEM, JEOL-2100F) equipped with the energy-dispersive X-ray spectroscopy (EDX). The crystalline structures of all samples were characterized by X-ray diffraction patterns (XRD, Rigaku D/max-2200V PC) using Cu K α radiation ($\lambda = 0.15403$ nm) from 10° to 90° at a rate of 8° min $^{-1}$. The layer thickness of graphite sheet was recorded by atomic force microscopy (AFM, Bruker Dimension Icon) after hydrofluoric acid etching of Si–G nanosheet. The chemical states of the Si–G nanosheet were measured on X-ray photoelectron spectra (XPS, Thermo Scientific Inc.) with Mg K α radiation ($\lambda = 0.9890$ nm). Conductivity evaluated on four-probe resistance tester ST2722-SD and high resistance instrument ST2643. And the specific surface area was tested by nitrogen adsorption–desorption isotherms on adsorptiometer (Quanta chrome Autosorb-1) using the Brunauer–Emmett–Teller (BET) method.

Electrochemical Measurement

To prepare electrode, Si–G microspheres, polyacrylic acid (PAA), acetylene black with the mass ratio of 75:15:10 were mixed into homogeneous slurry in deionized water. That slurry was coated on copper foil substrate, and then dried at 120 °C overnight in vacuum. The loading of active materials is 0.76 mg cm $^{-2}$. A coin-type cell (CR2032) was used with Si–G microsphere anode as the working electrode, lithium foil as the reference/counter electrode, Celgard 2300 Polyethylene (PE) as the separator, 1 M LiPF $_6$ dissolved in Ethylene carbonate/Ethyl methyl carbonate/Dimethyl carbonate (EC/EMC/DMC, 1:1:1, by volume) with 15% Fluoroethylene carbonate (FEC) as the electrolyte. The cell assembled was carried out in an Ar-filled glove box (H $_2$ O and O $_2$ concentration

<1 ppm). The electrode preparing and coin cell assembling of commercial Si and Si–G nanosheet were following the same procedure.

To assemble a pouch-type full battery, a Si–G microsphere mixed with graphite anode was coupled with a LiNi_{0.5}Co_{0.2}Mn_{0.3}O₂ (NCM523) cathode, which was prepared by coating the slurry of commercially available NCM523 on Al foil. The anode is consist of the active material (91.0 wt.%), conducting agent (5.0 wt.%, 0.2 wt.% Single-walled Carbon Nanotube (SWCNT) and 4.8 wt.% Super P (SP)) and binder (1.5 wt.% Carboxylmethyl Cellulose (CMC) and 2.5 wt.% Styrene Butadiene Rubber (SBR)). Active material is a mixture of 97.5 wt.% graphite and 2.5 wt.% Si–G microspheres. The compaction density of the cathode and anode is 1.7 g cm⁻³ and 3.4 g cm⁻³, respectively. Meanwhile, the pouch-type cell battery was used with CT50 as the separator, LBC421B33 (Shenzhen Capchem Technology Co., Ltd.) as the electrolyte. Details of pouch-type full battery composition parameters are listed in Table S1.

Cyclic voltammogram (CV) measurement was tested on a Gamry reference 600+ electrochemical workstation at a scanning rate of 0.5 mVs⁻¹ with a voltage range of 0.01–1.5 V (vs. Li/Li⁺) for 6 cycles. The cycling and rate performance of the coin cell were examined by LAND-CT 2001A test system with the voltage ranging from 0.01 V to 1.5 V, and the same test of pouch-type full battery was carried out on eight-channel battery tester BTS8-3 system from 3.0 V to 4.2 V ($T=25^{\circ}\text{C}$, $H\leq 15\%$). Electrochemical impedance spectra (EIS) were executed on an Autolab PGSTAT302 N electrochemical workstation in the frequency range from 100 kHz to 0.1 Hz at the amplitude of 5 mV.

Acknowledgements

The authors acknowledge the National Natural Science Foundation of China (Grant No. 52002238), Shanghai Municipal Science and Technology Commission (Grant No. 22ZR1423800, 21DZ2280600, 19DZ2293100) and Shanghai Municipal Education Commission.

Conflict of Interest

The authors declare no conflict of interest.

Data Availability Statement

The data that support the findings of this study are available on request from the corresponding author. The data are not publicly available due to privacy or ethical restrictions.

Keywords: anode • graphite • lithium-ion battery • microsphere • silicon

- [1] V. Etacheri, R. Marom, R. Elazari, G. Salitra, D. Aurbach, *Energy Environ. Sci.* **2011**, *4*, 3243–3262.
- [2] Z. P. Cano, D. Banham, S. Ye, A. Hintennach, J. Lu, M. Fowler, Z. Chen, *Nat. Energy* **2018**, *3*, 279–289.
- [3] G. Harper, R. Sommerville, E. Kendrick, L. Driscoll, P. Slater, R. Stolkin, A. Walton, P. Christensen, O. Heidrich, S. Lambert, A. Abbott, K. Ryder, L. Gaines, P. Anderson, *Nature* **2019**, *575*, 75–86.

- [4] X. Zuo, J. Zhu, P. Müller-Buschbaum, Y.-J. Cheng, *Nano Energy* **2017**, *31*, 113–143.
- [5] Y. Su, X. Feng, R. Zheng, Y. Lv, Z. Wang, Y. Zhao, L. Shi, S. Yuan, *ACS Nano* **2021**, *15*, 14570–14579.
- [6] Q. Wang, M. Zhu, G. Chen, N. Dudko, Y. Li, H. Liu, L. Shi, G. Wu, D. Zhang, *Adv. Mater.* **2022**, *34*, 2109658.
- [7] Y. Wu, G. Chen, Z. Wang, Y. Zhao, L. Shi, J. Zhu, M. Zhang, R. Jia, S. Yuan, *J. Energy Storage* **2018**, *17*, 102–108.
- [8] C. K. Chan, H. Peng, G. Liu, K. McIlwraith, X. F. Zhang, R. A. Huggins, Y. Cui, *Nat. Nanotechnol.* **2008**, *3*, 31–35.
- [9] H. Wu, G. Chan, J. W. Choi, I. Ryu, Y. Yao, M. T. McDowell, S. W. Lee, A. Jackson, Y. Yang, L. Hu, Y. Cui, *Nat. Nanotechnol.* **2012**, *7*, 310–315.
- [10] W. Wang, L. Gu, H. Qian, M. Zhao, X. Ding, X. Peng, J. Sha, Y. Wang, *J. Power Sources* **2016**, *307*, 410–415.
- [11] X. H. Liu, L. Zhong, S. Huang, S. X. Mao, T. Zhu, J. Y. Huang, *ACS Nano* **2012**, *6*, 1522–1531.
- [12] X. Zhuang, P. Song, G. Chen, L. Shi, Y. Wu, X. Tao, H. Liu, D. Zhang, *ACS Appl. Mater. Interfaces* **2017**, *9*, 28464–28472.
- [13] Y. Lv, M. Shang, X. Chen, P. S. Nezhad, J. Niu, *ACS Nano* **2019**, *13*, 12032–12041.
- [14] Z. Liu, Y. Zhao, R. He, W. Luo, J. Meng, Q. Yu, D. Zhao, L. Zhou, L. Mai, *Energy Storage Mater.* **2019**, *19*, 299–305.
- [15] M. Chen, Q. Zhou, J. Zai, A. Iqbal, T. Tsega, B. Dong, X. Liu, Y. Zhang, C. Yan, L. Zhao, A. Nazakat, S. E. C. Low, X. Qian, *Nano Res.* **2020**, *14*, 1004–1011.
- [16] G. Zhu, W. Jiang, J. Yang, *Chemistry* **2020**, *26*, 1488–1496.
- [17] Q. Shi, J. Zhou, S. Ullah, X. Yang, K. Tokarska, B. Trzebicka, H. Q. Ta, M. H. Rümmeli, *Energy Storage Mater.* **2021**, *34*, 735–754.
- [18] S. Chae, S. H. Choi, N. Kim, J. Sung, J. Cho, *Angew. Chem. Int. Ed.* **2020**, *59*, 110–135; *Angew. Chem.* **2020**, *132*, 112–138.
- [19] P. Li, H. Kim, S.-T. Myung, Y.-K. Sun, *Energy Storage Mater.* **2021**, *35*, 550–576.
- [20] J. Li, Y. Huang, W. Huang, J. Tao, F. Lv, R. Ye, Y. Lin, Y. Y. Li, Z. Huang, J. Lu, *Small* **2021**, *17*, 2006373.
- [21] Y. Luo, L. Huang, J. Liu, Z. Wang, Q. Chen, Y. Chen, *Microporous Mesoporous Mater.* **2022**, *331*, 111672.
- [22] Q. Xu, Q. Wang, D. Chen, Y. Zhong, Z. Wu, Y. Song, G. Wang, Y. Liu, B. Zhong, X. Guo, *Green Chem.* **2021**, *23*, 4531–4539.
- [23] M. H. Parekh, A. D. Sediako, A. Naseri, M. J. Thomson, V. G. Pol, *Adv. Energy Mater.* **2019**, *10*, 1902799.
- [24] N. Liu, H. Wu, M. T. McDowell, Y. Yao, C. Wang, Y. Cui, *Nano Lett.* **2012**, *12*, 3315–3321.
- [25] S. Li, Q. Li, R. W. Carpick, P. Gumbitsch, X. Z. Liu, X. Ding, J. Sun, J. Li, *Nature* **2016**, *539*, 541–545.
- [26] M. Chen, W. Cao, L. Wang, X. Ma, K. Han, *ACS Appl. Energ. Mater.* **2020**, *4*, 775–783.
- [27] X. Chen, Y. Xie, X. Xiong, K. Han, *Ionics* **2021**, *27*, 1013–1023.
- [28] H. Li, X. Li, D. Wang, S. Zhang, W. Xu, L. N. Zhu, L. Zhi, *Nanoscale* **2021**, *13*, 2820–2824.
- [29] B. Liu, P. Huang, M. Liu, Z. Xie, *J. Mater. Sci.* **2021**, *56*, 17682–17693.
- [30] L. Wang, F. Xi, Z. Zhang, S. Li, X. Chen, X. Wan, W. Ma, R. Deng, C. Chong, *Waste Manage.* **2021**, *132*, 56–63.
- [31] N. Wang, Y.-Y. Liu, Z.-X. Shi, Z.-L. Yu, H.-Y. Duan, S. Fang, J.-Y. Yang, X.-M. Wang, *Rare Met.* **2021**, *41*, 438–447.
- [32] Z.-Y. Wu, C.-Y. Wu, J.-G. Duh, *Mater. Lett.* **2021**, *296*, 129875.
- [33] S. J. Yeom, T. U. Wi, S. Ko, C. Park, K. Bayramova, S. Jin, S. W. Lee, H. W. Lee, *ACS Appl. Mater. Interfaces* **2022**, *14*, 5237–5246.
- [34] J. Zeng, N. Fu, X. Wang, A. a. Zhou, Z. Yang, *Appl. Surf. Sci.* **2021**, *557*, 149860.
- [35] S. Zhu, Y. Lin, Z. Yan, J. Jiang, D. Yang, N. Du, *Electrochim. Acta* **2021**, *377*, 138092.
- [36] D. Ruan, L. Wu, F. Wang, K. Du, Z. Zhang, K. Zou, X. Wu, G. Hu, J. *Electroanal. Chem.* **2021**, *884*, 115073.
- [37] C. Yu, X. Tian, Z. Xiong, Z. Zhang, Z. Sun, X. Piao, *J. Alloys Compd.* **2021**, *869*, 169124.

Manuscript received: April 21, 2022

Revised manuscript received: May 11, 2022

Accepted manuscript online: May 12, 2022

Version of record online: May 26, 2022